J|A|C|S ARTICLES

Published on Web 04/12/2010

Goldilocks Effect in Magnetic Bistability: Remote Substituent Modulation and Lattice Control of Photoinduced Valence Tautomerism and Light-Induced Thermal Hysteresis

R. D. Schmidt, D. A. Shultz,* J. D. Martin, and P. D. Boyle

Department of Chemistry, North Carolina State University, Raleigh, North Carolina 27695-8204

Received March 8, 2010; E-mail: Shultz@ncsu.edu; rdschmid@ncsu.edu; Jim_Martin@ncsu.edu; boyle@laue.chem.ncsu.edu

Abstract: The thermal-induced and photoinduced valence tautomerism of a series of Co(dioxolene)$_2$(4-X-py)$_2$ complexes (dioxolene = 3,5-di-*tert*-butylcatecholate or 3,5-di-*tert*-butylsemiquinonate; 4-X-py = 4-(X)pyridine, X = H (**1**), OMe (**2**), Me (**3**), CN (**4**), Br (**5**), NO_2 (**6**)) is described. The thermal valence tautomerism (*ls*-Co^{III}(SQ)(Cat)(4-X-py)$_2$ ↔ *hs*-Co^{II}(SQ)(SQ)(4-X-py)$_2$) is only observed for complexes **4**, **5**, and **6** where each is accompanied by a hysteresis loop of ca. 5 K. When a crystalline sample of **4**−**6** is held at 10 K in a SQUID magnetometer and irradiated with white light (λ = 400−850 nm), the *hs*-Co^{II} tautomer is formed. When the light source is removed, and the sample is slowly heated, the *hs*-Co^{II} tautomer persists until ca. 90 K, approximately 40 K higher than the thermal stability of previously reported complexes. Heating and cooling the sample while maintaining irradiation results in the appearance of a new light-induced thermal hysteresis loop below 90 K (ΔT = ca. 25 K). Below 50 K, the *hs*-Co^{II} tautomer displays temperature-independent relaxation to the *ls*-Co^{III} form, and above 50 K, the relaxation is thermally activated with an activation energy E_a > ca. 1500 cm^{-1}. The coordination geometry (trans-pyridines), pyridine substitution, and crystal packing forces conspire to create the comparatively thermally stable photogenerated *hs*-Co^{II} tautomer, thus providing an excellent handle for molecular and crystal engineering studies.

Introduction

Molecules demonstrating a reversible interconversion between redox isomers are called valence tautomers.[1,2] In cobalt dioxolene complexes, the resultant intramolecular electron transfer is generally accompanied by a spin-crossover at the cobalt ion.[1,2] The quintessential valence tautomeric equilibrium is the *ls*-Co^{III}(SQ)(Cat)L ↔ *hs*-Co^{II}(SQ)(SQ)L system, where SQ is a substituted *o*-semiquinonate, Cat is a substituted *o*-catecholate, and L is usually a redox innocent diamine ligand.[2] Several complexes of this type are known to demonstrate this valence reorganization in response to external stimuli, such as temperature and pressure, provided $\Delta H°$ is sufficiently small and $\Delta S°$ is sufficiently large such that $\Delta G°$ changes sign over the temperature range of the experiment.[2,3] In certain cases, when crystal packing permits changes in Co−O and Co−N bond lengths (ca. 0.15 Å increase in going from *ls*-Co^{III} to *hs*-Co^{II}),[3] the conversion of Co^{III} → Co^{II} → Co^{III} is accompanied by thermal hysteresis.[4] In some cases this conversion can be induced by irradiation of a Co^{III} charge transfer band to yield the Co^{II} form, which is metastable at temperatures sufficiently low enough to afford slow relaxation kinetics.[4–7] There exists only a handful of complexes reported that demonstrate this "photoinduced" valence tautomerism, presenting very small stability ranges (10−50 K), and decay begins as soon as the light stimulus is removed.[6,8−10] Moreover, those complexes shown to demonstrate this photoactivity lack a common structural feature that can be used as a molecular design element for systematically studying this phenomenon. Photoswitchable valence tautomers are therefore attractive bistable molecules that might have use in novel electronic or spintronic devices, and the preparation and characterization of new complexes that exhibit these properties is an important field of research if useful materials are to be realized.

A challenge to producing useful devices is preparing compounds that (1) exhibit cooperative intermolecular interactions that result in hysteresis and (2) demonstrate long-term thermal stability of the photogenerated tautomer.[6] We have recently reported such a complex, *ls*-Co^{III}(Cat)(SQ)L$_2$ (where L = 4-cyanopyridine, Cat/SQ = 3,5-di-*tert*-butylcatecholate/3,5-di-*tert*-butylsemiquinonate), demonstrating long-lived photoinduced valence tautomerism with a T_c of the photogenerated form of

(1) Shultz, D. A. Valence Tautomerism in Dioxolene Complexes of Cobalt. In *Magnetism: Molecules to Materials II*; Miller, J. S., Drillon, M., Eds.; Wiley-VCH: New York, 2001; Vol. 2, pp 281−306.
(2) Buchanan, R. M.; Pierpont, C. G. *J. Am. Chem. Soc.* **1980**, *102* (15), 4951–4957.
(3) Adams, D. M.; Dei, A.; Rheingold, A. L.; Hendrickson, D. N. *J. Am. Chem. Soc.* **1993**, *115* (18), 8221–8229.
(4) Tao, J.; Maruyama, H.; Sato, O. *J. Am. Chem. Soc.* **2006**, *128* (6), 1790–1791.
(5) Sato, O.; Hayami, S.; Gu, Z.-z.; Takahashi, K.; Nakajima, R.; Fujishima, A. *Phase Transitions* **2002**, *75* (7), 779–785.
(6) Sato, O.; Cui, A.; Matsuda, R.; Tao, J.; Hayami, S. *Acc. Chem. Res.* **2007**, *40* (5), 361–369.
(7) Cui, A.; Takahashi, K.; Fujishima, A.; Sato, O. *J. Photochem. Photobiol. A* **2004**, *167* (2−3), 69–73.
(8) Beni, A.; Dei, A.; Laschi, S.; Rizzitano, M.; Sorace, L. *Chem.−Eur. J.* **2008**, *14* (6), 1804–1813.
(9) Beni, A.; Dei, A.; Rizzitano, M.; Sorace, L. *Chem. Commun.* **2007**, 2160–2162.
(10) Carbonera, C.; Dei, A.; Létard, J.-F.; Sangregorio, C.; Sorace, L. *Inorg. Chim. Acta* **2007**, *360* (13), 3825–3828.

Scheme 1. Generic Complex in the *ls*-Co^{III}- (Left) and *hs*-Co^{II}- (Right) Forms

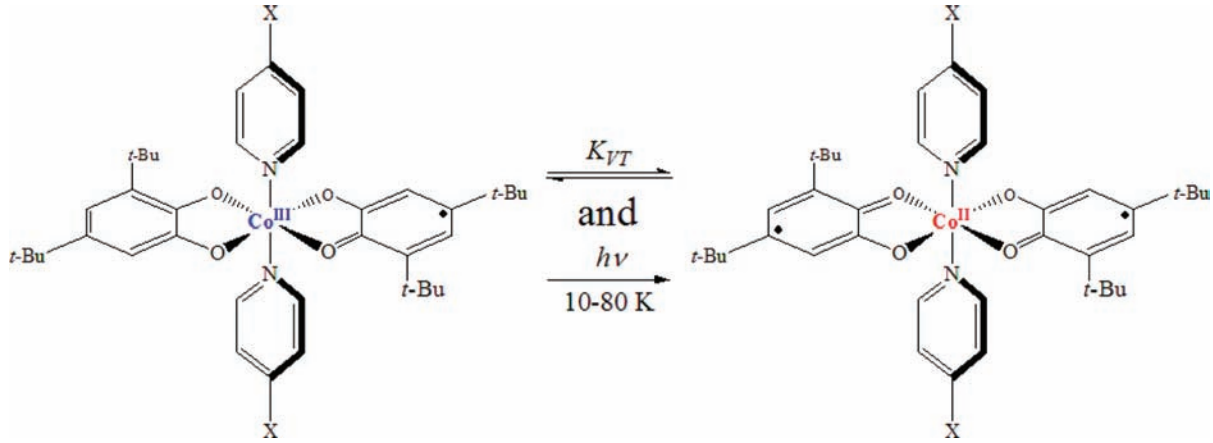

ca. 90 K and unmatched kinetic stability below ca. 50 K.[11] Herein, we expand on our study of these systems with a series of new complexes, **1**−**6**, that share a common structural topology and differ only in ancillary substituent, where complexes **1**−**3** persist as the *ls*-Co^{III} tautomer in response to temperature and light and complexes **4**−**6** exhibit both thermal conversion below 250 K and the stability of the photogenerated *hs*-Co^{II} tautomer (Scheme 1). Also explored are the consequences of cooperativity on the kinetic decay processes and the appearance of a light-induced thermal hysteresis (LITH) loop.[12,13] We propose that the coordination geometry (dioxolenes in the equatorial plane with axial-pyridines), the pyridine substituent, and crystal packing forces conspire to create the comparatively thermally stable photogenerated *hs*-Co^{II} tautomer, thus providing an excellent handle for molecular and crystal engineering studies.

Experimental Section

General Considerations. Elemental analyses (C, H, and N) were performed by Atlantic Microlab, Inc., Norcross, GA. Infrared spectra were collected on a Perkin-Elmer Spectrum RX-1 FT-IR spectrometer for samples cast as a film from CH_2Cl_2 on a NaCl plate. Unless noted otherwise, all reactions were performed in oven-dried glassware under a nitrogen atmosphere. Solvents were collected from an alumina column solvent purification system.[14] $[Co(SQ)_2]_4$,[15] 4-bromopyridine,[16] and 4-nitropyridine[17] were prepared according to published methods. The preparation of Co^{III}(3,5-DBSQ)(3,5-DBCat)(4-CN-py)$_2$ (**4**) has been previously reported.[11] Other reagents were used as received, without further purification. SQ = 3,5-di-*tert*-butyl-*o*-semiquinonate, Cat = 3,5-di-*tert*-butyl-*o*-catecholate.

Synthesis. (Co^{III}(SQ)(Cat)(py)$_2$) (1). To a 100 mL oven-dried Schlenk flask are added $[Co^{II}(SQ)_2]_4$ (500 mg, 0.25 mmol) and 30 mL of toluene, affording a green solution. To this mixture is added pyridine (0.16 mL, 2.00 mmol) neat via syringe. The reaction mixture is stirred, shielded from light, and heated to 35 °C for 6 h. Concentration of the dark blue mixture affords **1** as crystalline blue needles (247 mg, 38%). IR (film from CH_2Cl_2) ν in cm^{-1}: 6262, 4390, 3075, 2956, 2907, 2870, 1665, 1577, 1510, 1452, 1359, 1284, 1247, 1207, 1152, 1093, 1069, 1024, 985, 900, 856, 762, 695, 649. Anal. Calcd $C_{38}H_{50}CoN_2O_4 \cdot 0.5C_7H_8$: C, 70.97; H, 7.80; N, 3.94. Found: C, 70.42; H, 7.61; N, 3.79.

(Co^{III}(SQ)(Cat)(4-OMe-py)$_2$) (2). To a 100 mL oven-dried Schlenk flask are added $[Co^{II}(SQ)_2]_4$ (203 mg, 0.10 mmol) and 30 mL of toluene, affording a green solution. To this mixture is added 4-methoxypyridine (0.10 mL, 0.99 mmol) neat via syringe. The reaction mixture is stirred, shielded from light, and heated to 35 °C for 5 h. Concentration of the dark blue mixture affords **2** as a blue solid (207 mg, 72%). IR (film from CH_2Cl_2) ν in cm^{-1}: 6180, 3787, 2956, 2908, 2871, 1727, 1665, 1614, 1593, 1506, 1462, 1440, 1359, 1331, 1291, 1251, 1205, 1093, 1060, 1034, 986, 941, 902, 828, 733, 656, 583. Anal. Calcd $C_{40}H_{54}CoN_2O_6$: C, 66.93; H, 7.58; N, 3.90. Found: C, 66.68; H, 7.39; N, 5.01.

(Co^{III}(SQ)(Cat)(4-Me-py)$_2$) (3). To a 100 mL oven-dried Schlenk flask are added $[Co^{II}(SQ)_2]_4$ (61 mg, 0.03 mmol) and 25 mL of toluene, affording a green solution. To this mixture is added 4-methylpyridine (0.024 mL, 0.25 mmol) neat via syringe. The reaction mixture is stirred, shielded from light, and heated to 35 °C for 4 h. Concentration of the dark blue mixture affords **3** as a blue solid (68 mg, 79%). IR (film from CH_2Cl_2) ν in cm^{-1}: 6201, 3920, 3076, 2958, 2519, 1728, 1665, 1621, 1577, 1506, 1463, 1362, 1284, 1249, 1206, 1090, 1069, 1023, 986, 899, 856, 734, 683. Anal. Calcd $C_{40}H_{54}CoN_2O_4$: C, 70.05; H, 7.94; N, 4.08. Found: C, 69.33; H, 7.80; N, 3.45.

(Co^{III}(SQ)(Cat)(4-Br-py)$_2$) (5). To a 250 mL oven-dried Schlenk flask containing freshly prepared 4-bromopyridine (290 mg, 1.84 mmol) is added $[Co^{II}(SQ)_2]_4$ (459 mg, 0.23 mmol) in 50 mL of toluene, affording a blue-green solution. The reaction mixture is stirred, shielded from light, and heated to 35 °C for 5 h. Concentration of the dark blue mixture affords **5** as a blue solid (410 mg, 55%). IR (film from CH_2Cl_2) ν in cm^{-1}: 6165, 4109, 2959, 2908, 1730, 1668, 1584, 1472, 1412, 1360, 1287, 1246, 1203, 1093, 1055, 1020, 985, 902, 860, 814, 734, 701. Anal. Calcd $C_{38}H_{48}CoBr_2N_2O_4$: C, 55.96; H, 5.93; N 3.43. Found: C, 56.96; H, 6.12; N, 3.01.

(Co^{III}(SQ)(Cat)(4-NO_2-py)$_2$) (6). To a 100 mL oven-dried Schlenk flask are added $[Co^{II}(SQ)_2]_4$ (181 mg, 0.09 mmol) and 15 mL of toluene, affording a green solution. To this mixture is added 4-nitropyridine (90 mg, 0.73 mmol) as a solution in 15 mL of toluene. The reaction mixture is stirred, shielded from light, and heated to 35 °C for 6 h. Concentration of the dark blue mixture affords **6** as crystalline blue needles (57 mg, 21%). IR (film from CH_2Cl_2) ν in cm^{-1}: 3666, 3107, 2961, 1728, 1666, 1586, 1534, 1450, 1411, 1353, 1236, 1095, 1055, 1020, 983, 858, 744, 693.

(11) Schmidt, R. D.; Shultz, D. A.; Martin, J. D. *Inorg. Chem.* **2010**, *49* (7), 3162–3168.
(12) Létard, J.-F.; Guionneau, P.; Rabardel, L.; Howard, J. A. K.; Goeta, A. E.; Chasseau, D.; Kahn, O. *Inorg. Chem.* **1998**, *37* (17), 4432–4441.
(13) Desaix, A.; Roubeau, O.; Jeftic, J.; Haasnoot, J. G.; Boukheddaden, K.; Codjovi, E.; Linarès, J.; Noguès, M.; Varret, F. o. *Eur. Phys. J. B* **1998**, *6* (2), 183–193.
(14) Pangborn, A. B.; Giardello, M. A.; Grubbs, R. H.; Rosen, R. K.; Timmers, F. J. *Organometallics* **1996**, *15* (5), 1518–1520.
(15) Buchanan, R. M.; Fitzgerald, B. J.; Pierpont, C. G. *Inorg. Chem.* **1979**, *18* (12), 3439–3444.
(16) Heitz, W.; Rehder, A.; Nieβner, N. *Makromol. Chem., Rapid Commun.* **1991**, *12* (11), 637–643.
(17) Ochiai, E. *J. Org. Chem.* **1953**, *18* (5), 534–551.

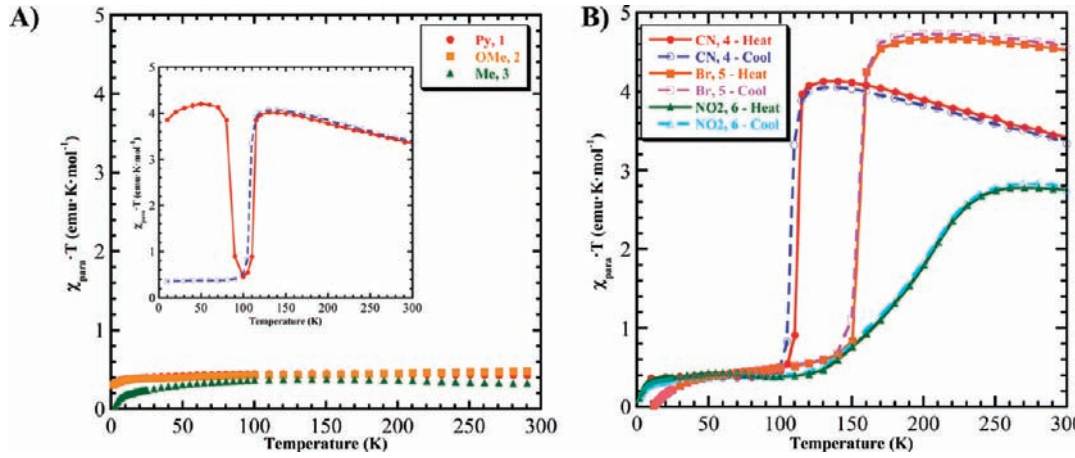

Figure 1. Variable-temperature magnetic susceptibility plotted as $\chi_{para}\cdot T$ vs T: (A) Heating curves for **1**−**3**; (B) Heating (filled) and Cooling (empty) curves for **4**−**6**. Inset: Illustrates first heating (●) and cooling (□) cycle for **4**; note disappearance of plateau.

Anal. Calcd $C_{38}H_{48}CoN_4O_8$: C, 61.04; H, 6.47; N, 7.49. Found: C, 59.51; H, 6.56; N, 6.15.

UV−vis Spectroscopy. Spectra were collected on an Agilent 8453 UV/vis spectrometer equipped with Hewlett-Packard UV/vis Chemstation Data Collection/Analysis software for samples prepared as solutions in CCl_4. Variable temperature UV−vis−NIR spectra were collected on a Shimadzu UV-3600 spectrometer equipped with UVProbe software for samples prepared as dilute polystyrene films (ca. 1.5 cm ×1.5 cm ×1 mm) and mounted in an Oxford Instruments optical cryostat (Project No. 38012) with quartz windows.

Magnetometry. Magnetic susceptibilities were measured on a Quantum Design MPMS-XL7 SQUID magnetometer with an applied field of 0.7 T for Curie plots. Microcrystalline samples (ca. 10−20 mg) were loaded into gelcap/straw sample holders and mounted to the sample rod with Kapton tape for temperature dependence measurements. Raw data from the gelcap samples were corrected for the sample container and molecular diamagnetism using Pascal's constants as a first approximation. The data were further corrected for inaccuracies in the diamagnetic correction by incorporation of a straight line, the slope of which represents the residual diamagnetic correction.

Photochemical Experiments. Magnetic susceptibilities were measured on a Quantum Design MPMS-XL7 SQUID Magnetometer with an applied field of 0.7 T for Curie plots. Crystalline samples (ca. 1.0 mg) were loaded into a quartz cup and placed into a Fiberglide Industries fiber optic rod assembly for photoexcitation experiments. The samples were photolyzed with a Dolan-Jenner Fiber-Lite Model 180 high intensity fiber optic illuminator, equipped with a tungsten-halogen EKE lamp (150 W, $\lambda = 400-850$ nm). The data for the fiber optic samples were corrected for the inherent diamagnetism of the sample holder through a background scan subtraction and for molecular diamagnetism through Pascal's constants.

X-ray Crystallography. X-ray crystallography for complexes **3**−**6** was conducted at the X-ray Structural Facility at North Carolina State University. Data collection and refinement for complexes **1** and **2** were conducted at the X-ray facility at the University of Michigan. A complete description of the crystallographic data and refinement details is reported in the Supporting Information.

Results and Discussion

The structural features of these complexes are heavily dependent on the electron distribution within the system (i.e., *ls*-Co^{III}(Cat)(SQ) vs *hs*-Co^{II}(SQ)(SQ)). As such, an initial discussion of the magnetic behavior is necessary, to establish the temperature stability ranges of each tautomeric form and highlight the dependence of the magnetic behavior on the solid state structure. This allows for a judicious selection of temperatures for X-ray data collection to ensure pure structures of the *ls*-Co^{III} and *hs*-Co^{II} forms and to avoid data collection at or near the $T_{1/2}$ of thermal conversion.

Variable-Temperature Magnetic Susceptibility. Figure 1 shows the paramagnetic susceptibility (χ_{para}) data for **1**−**3** (Figure 1A) and **4**−**6** (Figure 1B) plotted as the paramagnetic susceptibility temperature product, $\chi_{para}\cdot T$, vs temperature. In complexes **1**−**3** the value of $\chi_{para}\cdot T$ persists at 0.38 emu·K·mol^{-1}, consistent with the *ls*-Co^{III}(SQ)(Cat)(4-X-py)$_2$ charge distribution, over the temperature range 2−300 K (samples introduced at ca. 150 K then cooled to 2 K). Complexes **4**−**6**, however, reach a maximum value between 2.7 and 4.8 emu·K·mol^{-1}, consistent with the *hs*-Co^{II}(SQ)$_2$(4-X-py)$_2$ charge distribution. The differences in the maximum value of $\chi_{para}\cdot T$ likely arise from small changes in the weighted average *g*-value contribution from the Co^{II}. As the temperature is lowered, $\chi_{para}\cdot T$ decreases gradually and then somewhat sharply to again reach the minimum value of 0.38 emu·K·mol^{-1}. When **4**−**6** are subjected to thermal cycling over the range 2−300 K, the midpoint ($\gamma_{LS} = \gamma_{HS} = 0.5$; $T_{1/2}$) for increasing temperature differs from that for decreasing temperature. Thus, a thermal hysteresis loop exists for the thermal valence tautomerism of **4** (5 K), **5** (5 K), and **6** (5 K). The inset of Figure 1A shows the first thermal cycle collected for **4**, where a plateau below ca. 90 K is evident in the heating data; both **5** and **6** present this thermal quenching behavior, although at a much lower mole fraction. The disappearance of this plateau upon heating suggests that the sample was thermally trapped in the high temperature stable *hs*-Co^{II} form when quenched from room temperature (300 K) to 2 K. This observation provides evidence for metastability of the Co^{III}/Co^{II} species at temperatures below the decay temperature of ca. 90 K.[11] This type of behavior, although not light-induced, is reminiscent of iron-based spin-crossover complexes demonstrating the light-induced excited state spin-trapping (LIESST) effect.[12,18−21] This similarity prompted the notion of generating the metastable *hs*-Co^{II} species through photoexcitation rather than thermal quenching.

Another useful tool in probing valence tautomerism is variable-temperature optical spectroscopy, relying on the tem-

(18) Gütlich, P.; Garcia, Y.; Woike, T. *Coord. Chem. Rev.* **2001**, *219−221*, 839–879.
(19) Gütlich, P.; Hauser, A. *Coord. Chem. Rev.* **1990**, *97*, 1–22.

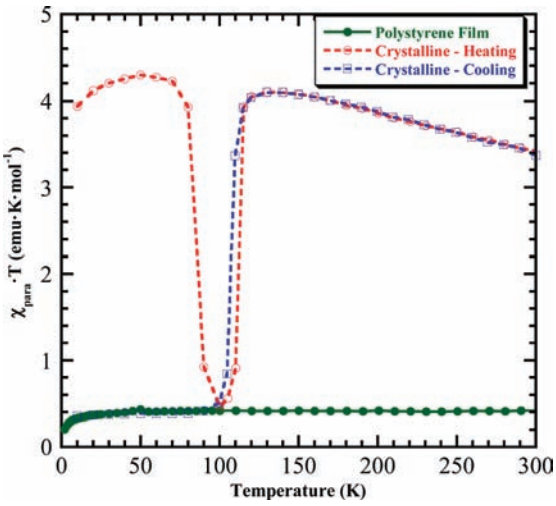

Figure 2. Variable-temperature behavior of a sample of **4** dispersed in a polystyrene matrix (ca. 2.0 wt %): magnetic susceptibility plotted as χ_{para}·T vs T with a plot of the crystalline sample for comparison.

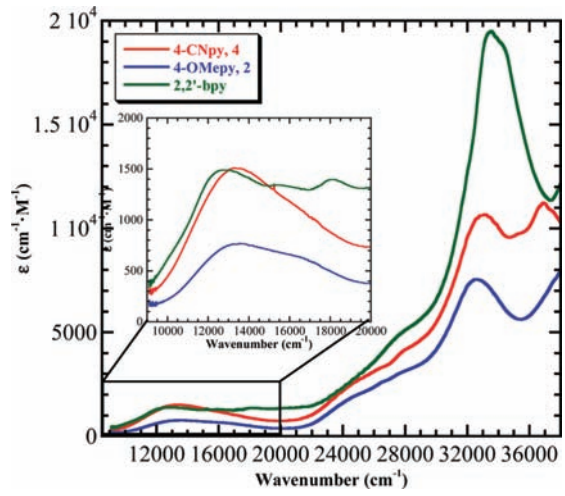

Figure 3. Electronic absorption spectra of **2** (blue) and **4** (red) in CCl_4 at 300 K (red). Reference spectrum of $Co^{II}(SQ)(SQ)(2,2'\text{-bpy})^2$ (green) included to highlight Co^{II} MLCT bands.

perature dependence of electronic absorption bands associated with either the *ls*-Co^{III} or *hs*-Co^{II} form, from which plots of optical density at the absorption maxima tend to follow the same behavior as shown in the solid state.[2,3,22,23] In some cases the solution-based conversion can be more gradual, as taking the system out of the solid state alleviates any crystal packing forces that can act to restrict the conversion of $Co^{III} \rightarrow Co^{II}$. These crystal forces can be strong enough to force the valence tautomeric conversion out of the measurement range, where the sample appears to be valence tautomeric in solution but not in the solid.[23,24] The solution data for **4**−**6**, however, suggest that these complexes are valence tautomeric only in the solid state. Variable-temperature electronic absorption spectra were collected on samples of **1**−**6** as a dilute solution (ca. 1−3 wt %) cast in a polystyrene film. These films were mounted into an optical cryostat in a Shimadzu UV-3600 UV−vis−NIR spectrometer, with data collected in the range 500−1600 nm (ca. 20 000−6000 cm^{-1}) over the temperature range 75−300 K (Supporting Information). There is little temperature dependence of any of the features of interest consistent with valence tautomerism, specifically the Co^{III} and Co^{II} metal−ligand charge transfer (MLCT) bands between ca. 10 000 and 20 000 cm^{-1}.[3,22]

As a verification of this result, the polymer sample of **4** was crushed and the variable-temperature magnetic susceptibility behavior was collected, representing the "solution" behavior, as the sample is suspended in a polymer matrix and crystalline forces are absent. The results of this experiment are presented in Figure 2, where there appears to be no observable valence tautomeric transition within the range 2−300 K, in stark contrast to the solid state behavior (shown for comparison), and the opposite of that expected based on other valence tautomeric systems.[23,24] This behavior is more consistent with that observed in **1**−**3**, as well as other nominally C_{2h}-symmetric cobalt valence tautomers, where the observed $T_{1/2}$ is above 350 K.[25] The origin of the absence of valence tautomeric behavior in solution is likely due to the importance of crystalline forces in facilitating the *ls*-$Co^{III} \rightarrow$ *hs*-Co^{II} conversion, *vide infra*.[11]

Photoinduced Valence Tautomerism. To test this metastable hypothesis, crystalline samples of **1**−**6** were held at 10 K in a SQUID magnetometer and irradiated with a light source; this photoexcitation has been demonstrated for **4**.[11] The common tool to probe the accessibility and stability of this metastable state is irradiation with a laser source.[5,8,12,18,20] Lacking access to a laser, this metastability was tested at 10 K by irradiation with a white light source (150 W, λ = 400−850 nm). Complexes **1**−**3** demonstrated no change in χ_{para}·T on the time scale of the experiment, so no observable conversion was achieved. Complexes **4**−**6** demonstrated a much different result, as the χ_{para}·T values began to rise sharply and then slowly from 0.38 to ca. 1.8 emu·K·mol^{-1}, consistent with a partial photochemical conversion to the metastable *hs*-Co^{II} form. Throughout the irradiation experiments, Co^{II} conversion percentages in a range of 15−30% were achieved for **4**−**6**, a significant increase relative to most previously reported examples of irradiation with single wavelength laser excitation, which commonly reached a photostationary limit.[6,7,9,10,26] In our experience, a photostationary limit was never achieved as the value of χ_{para}·T never plateaus and continues to grow (albeit at a very slow rate) even after 12 h of irradiation (see Supporting Information). This behavior could be attributed to the inability of the incident light to penetrate the samples fully due to the opacity of the crystalline material.[8] An alternate explanation for this is that the *hs*-Co^{II} form also absorbs in this wavelength range, which would result in a photoinduced decay process, and ultimately a steady-state would be reached.[7] Given both the large wavelength range used and the electronic absorption spectra of both tautomeric forms (Figure 3), this seems to be a reasonable explanation.[3,22]

Upon subsequent heating of the photogenerated species in **4**, the χ_{para}·T value achieved by 10 K irradiation persists until ca.

(20) Decurtins, S.; Gütlich, P.; Köhler, C. P.; Spiering, H.; Hauser, A. *Chem. Phys. Lett.* **1984**, *105* (1), 1–4.
(21) Breuning, E.; Ruben, M.; Lehn, J.-M.; Renz, F.; Garcia, Y.; Ksenofontov, V.; Gütlich, P.; Wegelius, E.; Rissanen, K. *Angew. Chem., Int. Ed.* **2000**, *39* (14), 2504–2507.
(22) Adams, D. M.; Hendrickson, D. N. *J. Am. Chem. Soc.* **1996**, *118* (46), 11515–11528.
(23) Evangelio, E.; Rodriguez-Blanco, C.; Coppel, Y.; Hendrickson, D. N.; Sutter, J. P.; Campo, J.; Ruiz-Molina, D. *Solid State Sci.* **2009**, *11* (4), 793–800.
(24) Caneschi, A.; Cornia, A.; Dei, A. *Inorg. Chem.* **1998**, *37* (13), 3419–3421.
(25) Kiriya, D.; Chang, H.-C.; Kitagawa, S. *J. Am. Chem. Soc.* **2008**, *130* (16), 5515–5522.
(26) Dapporto, P.; Dei, A.; Poneti, G.; Sorace, L. *Chem.—Eur. J.* **2008**, *14* (35), 10915–10918.

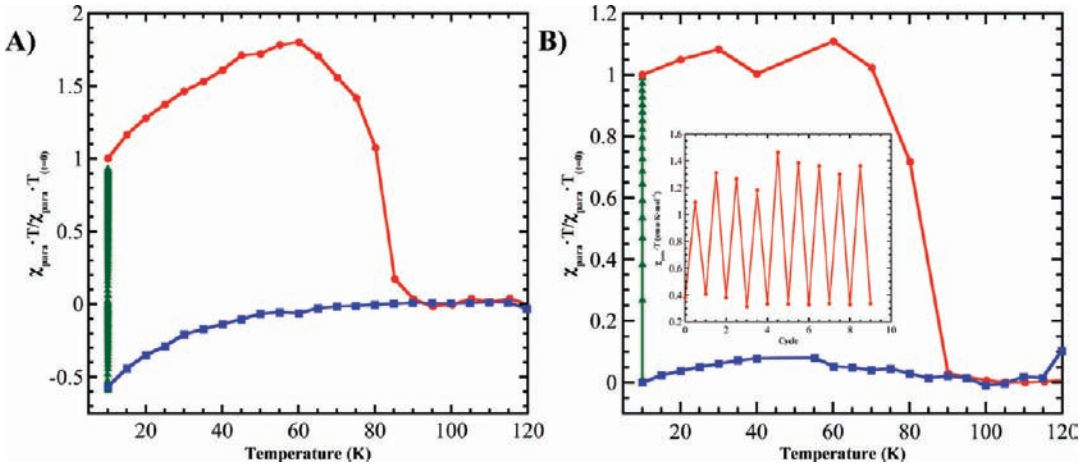

Figure 4. Photogeneration/thermal decay cycles of the *hs*-Co^{II}-form of **5** (A) and **6** (B) from 10−120 K depicting heating (●), cooling (■), and holding (▲) scans. Inset: Irradiation/thermal cycles of **4**.

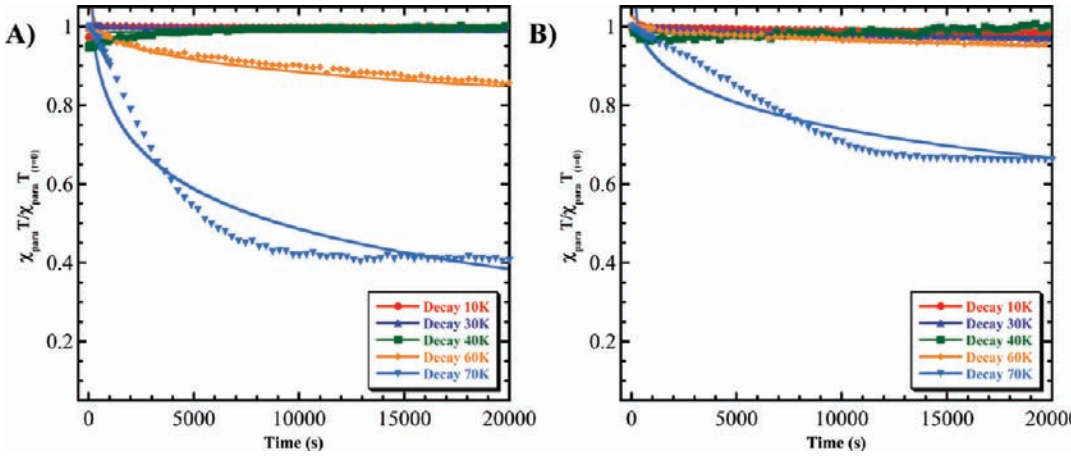

Figure 5. Decay kinetics of the photogenerated species for **5** (A) and **6** (B) from 10 to 70 K. The lines represent the best fit to eq 1 (stretched exponential).

90 K and can be regenerated by an additional irradiation cycle.[11] This behavior was also observed in **5** and **6**, with a single photogeneration/thermal decay cycle presented in Figure 4; the downturn in the data for **5** is representative of a very strong intermolecular antiferromagnetic interaction (θ). In comparison to all other compounds that undergo photoinduced valence tautomerism, these complexes exhibit far greater thermal stability of the photogenerated *hs*-Co^{II}-form.[6,9,27] In addition, **4**−**6** can be subjected to thermal cycling[7,28] (Figure 4A inset), suggesting that irradiation and thermal quenching do not result in appreciable decomposition. Interestingly, both the onset and behavior of the decay are the same irrespective of the substituent and strikingly similar to the thermal decay of the thermally quenched fraction, suggesting that the photoinduced behavior is independent of the withdrawing nature of the substituent. However, the thermal conversion for these complexes does change with the substituent, in both the onset and slope. This validates the notion that the thermal and photoinduced phenomena are inherently different behaviors.[9] Although the mechanisms governing the behaviors may differ, the presence of both the thermal conversion and photoinduced activity appears inherently linked to the crystalline lattice. It also appears that the ability to thermally quench a nonzero mole fraction of the high-temperature stable *hs*-Co^{II} form is an indicator of photoinduced activity.

Photogenerated *hs*-Co^{II} → *ls*-Co^{III} Relaxation. To compare the kinetic stability of the photogenerated form to that of other valence tautomers, the decay kinetics of the $\chi_{para}\cdot T$ values at several different temperatures was measured for **5** and **6** (Figure 5). Previously we reported the decay kinetics for **4** in comparison to other previously reported valence tautomers by attempting to fit the decay curves to a stretched exponential (eq 1) where $\chi_{para}\cdot T$ has its usual meaning, $\chi_{para}\cdot T_{(t=0)}$ is the value of $\chi_{para}\cdot T$ measured immediately after the light source is switched off, k is the rate constant for decay ($\tau = k^{-1}$), t is time, and β is a parameter that accounts for a distribution of species that exhibit different decay kinetics.[6,9,11,27,29] A value of $\beta = 0.3$ is most commonly used for similar systems.[28,29]

$$\frac{\chi_{para}\cdot T}{\chi_{para}\cdot T_{(t=0)}} = e^{(-kt)^{\beta}} \qquad (1)$$

However, the exponential fits suffer from unreliable lifetime values due to the high kinetic stability and near linear behavior on this time scale (ca. 30 000 s). This is also very apparent in

(27) Li, B.; Tao, J.; Sun, H.; Sato, O.; Huang, R.-B.; Zheng, L.-S. *Chem. Commun.* **2008**, (19), 2269–2271.
(28) Beni, A.; Dei, A.; Shultz, D. A.; Sorace, L. *Chem. Phys. Lett.* **2006**, *428* (4−6), 400–404.
(29) Carbonera, C.; Dei, A.; Sangregorio, C.; Létard, J.-F. *Chem. Phys. Lett.* **2004**, *396* (1−3), 198–201.

Table 1. Summary of Lifetimes Calculated for Complexes **4**−**6** and Comparison to Literature Values

Temperature (K)	Lower Limit:[11] VT-CNpy, **4**, τ (s)[a]	Lower Limit: VT-Brpy, **5**, τ (s)[a]	Lower Limit: VT-NO_2py, **6**, τ (s)[a]	Lit. τ (s)[9,27]	Lower Limit: Lit. τ (s)
10	1.6×10^6	8.1×10^6	2.0×10^6	2.0×10^{6b}	3.5×10^{5b}
				8.2×10^{6c}	2.9×10^{5c}
20	1.2×10^6			4.0×10^{6b}	1.9×10^{5b}
				2.2×10^{6c}	1.6×10^{5c}
30	5.8×10^5	3.7×10^6	9.3×10^5	9.1×10^{5b}	1.3×10^{5b}
40	2.0×10^5	–	–	3.6×10^{5b}	9.2×10^{4b}
				1.7×10^{5c}	5.6×10^{4c}
50	1.3×10^5			1.1×10^{5b}	5.0×10^{4b}
				4.9×10^{4c}	2.7×10^{4c}
60	1.2×10^4	1.6×10^5	7.2×10^5	6.3×10^{4b}	3.7×10^{4b}
70				2.3×10^{4b}	2.2×10^{4b}
80	5.4×10^3	2.7×10^4	6.5×10^4		

[a] Near linear decay behavior suggesting indefinite stability and unreliable fits to a stretched exponential.[30–32] [b] Taken from ref 27. [c] Taken from ref 9.

the high temperature (70 K) fits, which are very poor, suggesting another decay mechanism may be in operation. As such, for comparison purposes we were forced to abandon the unrealistic fit parameters and instead rely on an estimate of the lower limit on the decay lifetime based on the final decay percentage and experimental time scale. The results of the comparative analysis for **4**−**6** are presented in Table 1, along with the stretched exponential fit and estimated lower limit values from the literature.[9,27] The limiting values were calculated from rearrangement of eq 1 and the exclusion of β, from the final decay percentage (estimated for literature data) and the time scale of the experiment.

$$\tau = -\frac{t}{\ln\left(\frac{\chi_{para}\cdot T}{(\chi_{para}\cdot T)_{t=0}}\right)} \qquad (2)$$

The values calculated for the decay lifetimes below 50 K for **4**−**6** are significantly larger than any previously reported example at any temperature.[6,9]

Comparison of the new lower limiting values of the lifetimes suggests that complexes **4**−**6** demonstrate greater stability of at least an order of magnitude over these previously reported examples. Given that this new lower limit analysis suggests a 10 K lifetime of 1.6×10^6 s, a second decay trace of the photogenerated fraction of **4** at 10 K was collected, shown in Figure 6. This plot shows that the value of $\chi_{para}\cdot T$ is essentially unchanged, within instrumental error, over 5.6×10^5 s, supporting the supposition of indefinite stability, and actually suggests that the original fit of 4×10^{10} s may in fact be an underestimate of the real lifetime.

The rate constants (k) obtained from fits of the data in Figure 5 to eq 1 for **4**−**6** were used to construct Arrhenius plots, as shown in Figure 7, and fit using eq 3.[7,28,30–32]

$$\ln k = \ln A - \left(\frac{E_a}{k_B}\right)\left(\frac{1}{T}\right) \qquad (3)$$

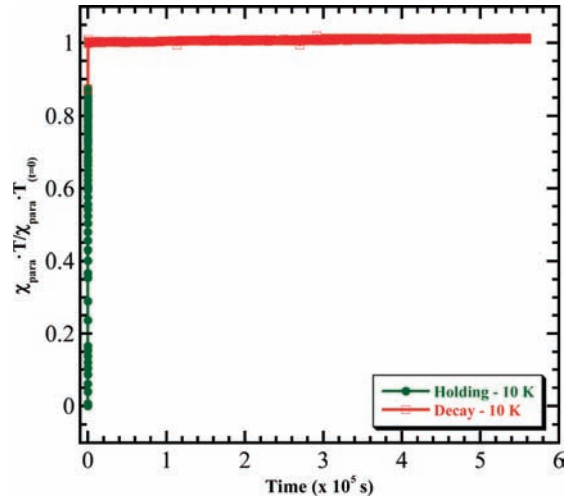

Figure 6. Decay of photogenerated *hs*-Co^{II} form of **4** over 6 days demonstrating stability.

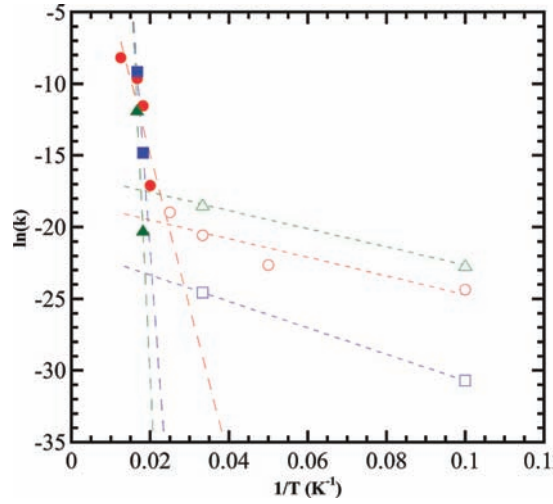

Figure 7. Arrhenius plots for **4** (●/○), **5** (■/□), and **6** (▲/△).

The data show a region below ca. 40 K where the rate constant is nearly temperature independent and a heavily temperature-dependent regime above 50 K. The data below 40 K are typical for decay due solely to quantum tunneling,[7,28] while the data above 50 K can be fit to a straight line; the results of this fit routine are summarized in Table 2.

The photoinduced activity, as well as the shape of the magnetic behavior, strongly resembles LIESST-based behavior

(30) Lifetime from fit to stretched exponential (eq 1) for **4**: 10 K, ca. 4×10^{10} s; 20 K, ca. 7×10^9 s; 30 K, ca. 9×10^8 s; 40 K, ca. 2×10^8 s; 50 K, ca. 3×10^7 s; 60 K, ca. 2×10^4 s; 80 K, 4×10^3 s.

(31) Lifetime from fit to stretched exponential (eq 1) for **5**: 10 K, ca. 2×10^{13} s; 30 K, ca. 5×10^{10} s; 40 K, ca. 2×10^{13} s; 60 K, ca. 3×10^6 s; 80 K, 9×10^3 s.

(32) Lifetime from fit to stretched exponential (eq 1) for **6**: 10 K, ca. 7×10^9 s; 30 K, ca. 1×10^8 s; 40 K, ca. 3×10^{10} s; 60 K, ca. 6×10^8 s; 80 K, 1×10^5 s.

Table 2. Arrhenius Plot Fit Parameters for **4**−**6**

	4		**5**[a]		**6**[a]	
Parameter	10−40 K	50−80 K	10−40 K	50−80 K	10−40 K	50−80 K
E_A (cm^{-1})	94	1525	132	−	92	−
A (s^{-1})	1.3×10^{-8}	507	4.6×10^{-10}	−	8.3×10^{-8}	−

[a] Insufficient data to obtain reasonable fit parameters.

in iron spin crossover complexes.[12,18–20,33–36] The plateau in $\chi_{para} \cdot T$ from ca. 10−70 K is reminiscent of the behavior and stability observed in these iron systems[12,33–36] and is in stark contrast to the behavior observed for the more closely related photoinduced valence tautomeric systems.[6,7,9,10,28,29,37] When compared directly to such systems, the thermal stabilities we observe appear dwarfed by these iron based systems. However, it is important to note that in these iron systems, the conversion is generally built around an Fe^{II} spin crossover (*ls*-$S_T = 0$, $^1A_1$; *hs*-$S_T = 2$, $^5T_2$) which provides a spin-forbidden decay mechanism enhancing thermal stability.[20,35,38] Our systems are unique in that there is no obvious spin forbidden pathway to decay in the conversion from *ls*-Co^{III}(Cat)(SQ) → *hs*-Co^{II}(SQ)(SQ) ($S_{Co(III)} = {}^1/_2$; $S_{Co(II)} = {}^5/_2$, ${}^3/_2$, ${}^3/_2$, ${}^1/_2$). The accessibility of an $S = {}^1/_2$ state in the *hs*-Co^{II} system provides a spin-allowed mechanism for decay to the *ls*-Co^{III}.

Thermally Quenched *hs*-Co^{II} → *ls*-Co^{III} Relaxation. The spin-crossover LIESST complexes generally present very strong cooperativity in the magnetic behavior, which is manifest in a sharp thermal decay at T_{LIESST}, precipitous thermal conversion accompanied by hysteresis, and a self-acceleration to the kinetic decay process.[12,13,18–20,33–36,39–41] Complexes **4**−**6** have already been shown to demonstrate both low temperature stability of the photogenerated/thermally quenched form with rapid thermal decay at T_{decay} and rapid thermal conversion accompanied by hysteresis, so the presence of self-accelerated decay must be investigated. Self-accelerated decay processes in iron spin-crossover complexes generally present very long kinetic stability ($k = \sim 10^{-6}$) until approaching the critical temperature (T_{LIESST}) at which point the decay becomes exponentially more rapid within a very short temperature range.[13,39–41] This decay process is generally described by a product of exponentials (eq 4): one dependent on the activation barrier (E_a) and one dependent on the high spin mole fraction and a self-acceleration parameter, $\alpha(T)$.[13,39–41] Fitting to the decay curves affords the self-acceleration parameter which can be useful in other photochemical experiments.

$$k_{HL}(T, \gamma_{hs}) = k^0_{HL}(T) e^{\left(\frac{E_a}{k_B T}\right)} e^{(-\alpha(T)\gamma_{hs})} \quad (4)$$

Given the similarity of the photoinduced behaviors to LIESST complexes, further kinetic analyses were conducted on **4** to investigate the kinetic decay rates of the thermally quenched fraction, representative of decay from 100% *hs*-Co^{II}. Figure 8 depicts the kinetic decay behavior of thermally quenched samples of **4** (i.e., 100% *hs*-Co^{II}) at temperatures approaching the onset of thermal decay at ca. 90 K. Those curves below 40 K present essentially indefinite stability over the time scale of the experiment (ca. 30 000 s), where the self-accelerated decay begins at ca. 70 K with sigmoidal behavior. At 75 and 80 K, complete decay of the *hs*-Co^{II} to *ls*-Co^{III} is observed within the experiment time, presenting a sigmoidal, self-accelerated decay process which rapidly decays at temperatures near 80 K.

This now confirms that complex **4** obeys self-accelerated decay rather than a stretched exponential decay process, which is consistent with the poor fits to the stretched exponential.[11,30] This behavior also helps to explain the shape of the high temperature decay traces for **5** and **6** (Figure 5), where the 70 K plots for both have very sharp slopes ending in near baseline behavior, similar to the behavior of **4** in Figure 8 below the point of sigmoidal inflection (ca. 40%) at 80 K. Given that conversion percentages of ca. 30% were achieved, the behavior for **5** and **6** is consistent with that observed for self-accelerated decay.

An important question to be posed given the comparison of the thermally quenched behavior with the photoinduced behavior is the nature of both species. The photoinduced species is assumed to be the same as the thermally quenched form, which is the *hs*-Co^{II}(SQ)(SQ) complex, although it is not certain. From the kinetic decay traces of the photogenerated forms, which resemble the low mole fraction portion (<30%) of the full decay curves, it is apparent that they follow the same behavior, yet resemble an exponential decay process. It appears then that the decay behavior is strongly dependent upon the initial mole fraction of *hs*-Co^{II} present, where, at levels below ca. 30−50%, the decay resembles exponential decay. To test this, a sample of **4** was subjected to a variable thermal quench decay experiment, in which the sample was quenched from 300 K → 80 K in ca. 5 s and then held for a set period of time to decay a portion of the sample before rapidly cooling the sample to 10 K (10 K/min, ca. 8.5 min) to freeze the decay process. The moment is measured at 10 K to estimate the mole fraction of *hs*-Co^{II} present, before heating again to 80 K to monitor the decay. Three of these variable quench cycles were collected, with 80 K hold times of 0, 12, and 25 min resulting in quenched fractions at 80 K of 95%, 68%, and 33%, respectively. The decay traces of each of these are presented in Figure 9A, along with the 100% *hs*-Co^{II} thermal quench curve and photogenerated decay curve (ca. 5% *hs*-Co^{II}).

It is clear from the decay behavior that as the concentration of *hs*-Co^{II} decreases, the sigmoidal behavior is more difficult to observe and the data begin to appear more exponential. What is very revealing is the superposition of all five decay curves (Figure 9B), where each variable curve falls perfectly along the 100% decay curve. This is to be expected, given they all originate from the same initial species. The most important result here is the overlap of the photogenerated curve with the 100% curve, which now links the photogenerated species behavior with the thermally quenched species behavior, providing strong evidence that they are both the same species.

(33) Capes, L.; Létard, J.-F.; Kahn, O. *Chem.—Eur. J.* **2000**, *6* (12), 2246–2255.
(34) Létard, J.-F.; Capes, L.; Chastanet, G.; Moliner, N.; Létard, S.; Real, J.-A.; Kahn, O. *Chem. Phys. Lett.* **1999**, *313* (1−2), 115–120.
(35) Li, D.; Clerac, R.; Roubeau, O.; Harte, E.; Mathoniere, C.; Le Bris, R.; Holmes, S. M. *J. Am. Chem. Soc.* **2007**, *130* (1), 252–258.
(36) Mishra, V.; Mukherjee, R.; Linares, J.; Balde, C.; Desplanches, C.; Létard, J.-F.; Collet, E.; Toupet, L.; Castro, M.; Varret, F. *Inorg. Chem.* **2008**, *47* (17), 7577–7587.
(37) Beni, A.; Carbonera, C.; Dei, A.; Létard, J.-F.; Righini, R.; Sangregorio, C.; Sorace, L. *J. Braz. Chem. Soc.* **2006**, *17* (8), 1522.
(38) Decurtins, S.; Gutlich, P.; Hasselbach, K. M.; Hauser, A.; Spiering, H. *Inorg. Chem.* **1985**, *24* (14), 2174–2178.
(39) Parreira, C.; Enachescu, C.; Linarès, J.; Boukheddaden, K.; Varret, F. *J. Phys.: Condens. Matter* **2000**, *12* (45), 9395–9406.
(40) Stassen, A. F.; Roubeau, O.; Ferrero Gramage, I.; Linarès, J.; Varret, F.; Mutikainen, I.; Turpeinen, U.; Haasnoot, J. G.; Reedijk, J. *Polyhedron* **2001**, *20* (11−14), 1699–1707.
(41) Hauser, A. *Chem. Phys. Lett.* **1992**, *192* (1), 65–70.

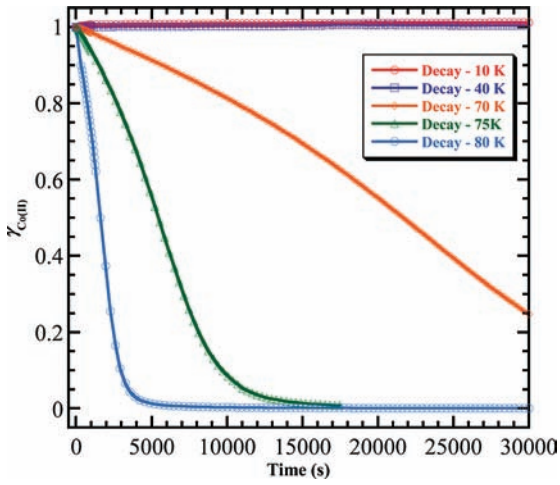

Figure 8. Decay of the mole fraction *hs*-Co^{II} ($\gamma_{Co(II)}$) for thermally quenched samples of **4** from 10 to 80 K. Significant self-acceleration begins at ca. 75 K.

Light-Induced Thermal Hysteresis. Light-induced thermal hysteresis (LITH) is a unique phenomenon currently only observed in certain iron-based spin-crossover LIESST systems and is limited to only those systems demonstrating photoinduced magnetization behaviors obeying self-accelerated decay processes, and has yet to be observed in a photoinduced valence tautomeric system.[12,13,33,39–42] LITH is characterized by the appearance of a new thermal hysteresis loop within the photoinduced (LIESST) region following photogeneration during thermal cycles under constant irradiation ("ON" mode), compared to thermal cycles under no irradiation ("OFF" mode, Figure 10). The importance of the self-accelerated decay condition is that the decay then follows different kinetics than the photoexcitation process, giving rise to two different steady states when starting from *hs*-Co^{II} (warming) or *ls*-Co^{III} (cooling). The LITH cycle is a purely kinetic phenomenon that speaks to the strong cooperativity in the light-induced *hs*-state.[12,13,33,38–43]

The photogeneration/thermal cycling shown in Figure 10 was repeated where the irradiation was maintained throughout both the heating and cooling cycles (ON mode), to see if there was any change in the behavior consistent with LITH, presented in Figure 11A. An initial cooling scan from 150 K is included for reference of the *ls*-Co^{III} baseline. Three cycles are shown, with the first following 1.5 h of irradiation at 10 K. Notably, the heating behavior appears to be similar to the OFF mode, with the exception of an increase in the converted portion. With continuous irradiation, there is a possibility of local heating of the sample, which would be manifest in a gradual decrease in the value of $\chi_{para}\cdot T$, contrary to experiment. This observed increase is therefore attributed to a greater irradiation time, consistent with other examples of LITH.[12,33] The major difference is the increase in the $\chi_{para}\cdot T$ value in the cooling regime, which gives rise to a new hysteresis loop with a ΔT of ca. 25 K. The data presented in Figure 11A were collected at a rate of 2 K/min, so the rate was decreased to 0.1 K/min and recollected to confirm that the behavior was real LITH (Figure 11B) and not a manifestation of photoexcitation over the time of irradiation during the cooling cycle. A final scan at 0.05 K/min (not shown) demonstrated little deviation from the 0.1 K/min data set. This similarity in behavior at all rates clearly shows that the hysteresis loops in Figure 11A and B are real and not mere artifacts of the cooling rate during irradiation. This effect is the manifestation of LITH and represents the first such example in a photoinduced cobalt valence tautomeric system. It should be pointed out that the LITH cycles were observed in samples converted to ca. 30% *hs*-Co^{II}, and as such LITH is unexpected given the dependence of self-accelerated decay on high concentrations (>ca. 70%) of *hs*-Co^{II}.[47] The observation of LITH, despite the small total conversion, is probably attributable to a surface effect where a conversion gradient is established through the crystals, with complete conversion (100%) at the surface, giving rise to the observed LITH, and minimal conversion (>30%) toward the center due to penetration depth of the light.[47,48]

The LITH effect is quite pronounced, with ca. 50 K < $T_{1/2}$ < 90 K. A simple explanation on the origin of the LITH curve has been proposed where, under constant irradiation, two kinetic processes are operable: photoinduced trapping of the *hs*-Co^{II} state and self-accelerated relaxation to the *ls*-Co^{III} ground state.[12] When $T > T_{decay}$, the relaxation rate dominates, and photoinduced trapping cannot be observed within the experimental time scale. However, when $T < T_{decay}$, the photoinduced trapping rate becomes dominant, resulting in an increase in $\chi_{para}\cdot T$ to some steady state value.[12,33] To confirm this LITH effect and a difference in steady states, irradiation experiments were performed at temperatures below the T_{decay}, to observe the maximum conversion at each temperature.[12] The results of this experiment are summarized in Figure 12, where a LITH cooling curve is included for reference. Each of the irradiation points (10, 40, 70, and 80 K) reaches a maximum coincident with, or just below, the LITH cooling curve. This shows that the maximum attainable steady-state for irradiation at a given temperature is consistent with the LITH curve, which was collected at 2 K/min over ~1.5 h.

Additionally, plots of $\chi_{para}\cdot T$ vs time (Supporting Information) for each temperature illustrate the evolution of $\chi_{para}\cdot T$ during the irradiation period (ca. 1.5 h). The 10 K excitation never reaches a steady state and continues to increase with time. The 40 K irradiation curve does not quite reach the steady-state value in 1.5 h, consistent with an observed maximum conversion value just below the LITH curve. Both the 70 and 80 K curves do, however, present a steady state, where the 70 K curve plateaus but the 80 K curve begins to be dominated by the thermal decay rate after only a few minutes.

As a final check of the rate competition inherent to the LITH process, the photostationary decay rate and photogeneration rates can be compared at a single temperature; 40 K was selected as the best example.[33] First, the sample is irradiated at 10 K (ca. 10 h), warmed to 40 K under irradiation, and then held at that temperature while the decay of $\chi_{para}\cdot T$ is monitored following removal of the light source. The sample is then warmed to 100 K to erase the *hs*-Co^{II} fraction, to ensure 100% *ls*-Co^{III}, before cooling to 40 K. The light source is turned on, and the sample

(42) Weber, B.; Kaps, E.; Weigand, J.; Carbonera, C.; Letard, J.-F.; Achterhold, K.; Parak, F. G. *Inorg. Chem.* **2007**, *47* (2), 487–496.
(43) Moliner, N.; Muñoz, M. C.; Létard, S.; Létard, J.-F.; Solans, X.; Burriel, R.; Castro, M.; Kahn, O.; Real, J. A. *Inorg. Chim. Acta* **1999**, *291* (1−2), 279–288.
(44) *CRC Handbook of Chemistry and Physics*, 88th ed.; CRC Press, Taylor & Francis Group: New York, 2008.
(45) Gregory, S. *Phys. Rev. Lett.* **1978**, *40* (11), 723.
(46) *Oxygen Contamination*; MPMS 1014-210; Quantum Design: San Diego, CA, 1997.
(47) We thank Prof. Andreas Hauser for pointing out this behavior.
(48) Varret, F.; Constant-Machado, H.; Dormann, J. L.; Goujon, A.; Jeftic, J.; Noguès, M.; Bousseksou, A.; Klokishner, S.; Dolbecq, A.; Verdaguer, M. *Hyperfine Interact.* **1998**, *113*, 37–46.

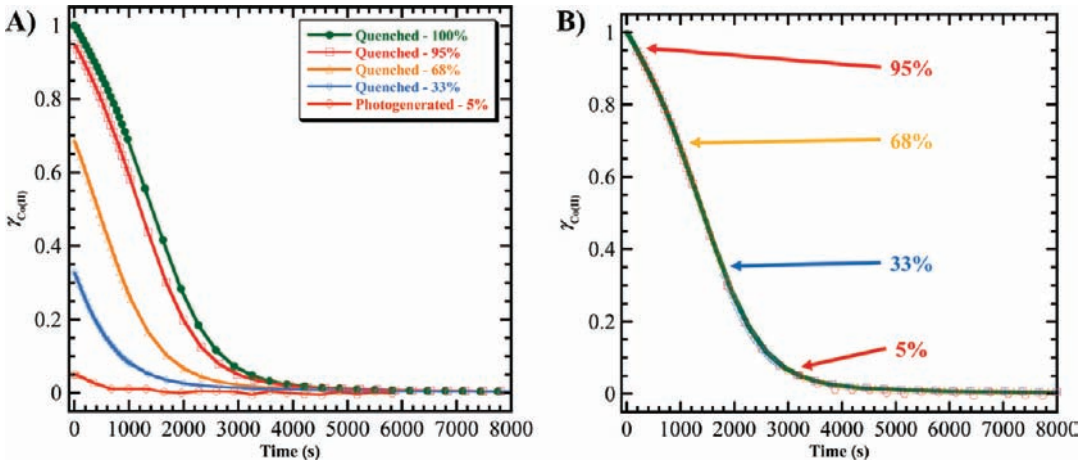

Figure 9. Decay of the mole fraction *hs*-Co^{II} ($\gamma_{Co(II)}$) for thermally quenched samples of **4** at 80 K from different initial concentrations of *hs*-Co^{II}: (A) overlay of all curves, (B) superposition of curves.

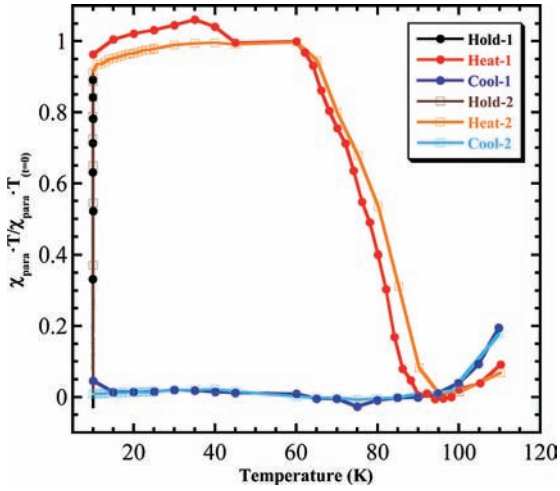

Figure 10. Photogeneration/thermal decay cycles of the *hs*-Co^{II}-form of **4** from 10 to 110 K (2 K/min rate). The data from 45 to 55 K are obscured due to a phase transition in oxygen trapped in the sample cavity and have been omitted.[44–46]

irradiated at 40 K while the increase of $\chi_{para}\cdot T$ is monitored. These curves are presented in the Supporting Information, illustrating the different steady-state values.

Finally, as the behaviors of **4**−**6** are very similar in this low temperature region, with each demonstrating similar responses to photoexcitation, the LITH cycle experiment was attempted on a sample of **6** (Figure 13). The results of this experiment were very similar to that observed for **4** with data collected at a rate of 2 K/min.

Molecular and Solid State Structure. As the photoinduced behavior appears to be independent of the substituent, one possible explanation for the observed behavior can be found in the macromolecular lattice packing. Figure 14 shows the ORTEP structures of complexes **1**−**3**, **5**, and **6**. In all of the structures, the cobalt sits on a crystallographically imposed inversion center, coincident with the molecular C_2 axis, resulting in averaged bond distances. As such, X-ray crystallography cannot distinguish between averaged bond lengths due to positional disorder and mixed-valent (Cat/SQ) delocalization; inspection of these bond lengths can merely confirm the [Co^{III}(diox)$_2$] or [Co^{II}(diox)$_2$] oxidation state.

During the conversion from *ls*-Co^{III} to *hs*-Co^{II} the Co-L bond lengths expand by an average of 0.15 Å.[3] At low temperatures, the crystalline lattice must be soft enough to accommodate this molecular expansion, yet hard enough to provide a mechanism for stability through close contacts. When the lattice is harder and very tightly packed, there is a strong resistance to expansion of the coordination sphere through tight intermolecular close contacts. In this case the complex would be expected to remain in the *ls*-Co^{III} form in response to photostimulus, with no observable conversion. In the limit of a very soft lattice, where there is a large intermolecular separation and fewer, longer molecular contacts, the lattice may accommodate the molecular expansion but lacks any mechanism for the complex to remain or "stick" in the expanded coordination sphere. In this case the complex may convert to the *hs*-Co^{II} form under irradiation but would rapidly relax to the *ls*-Co^{III} form on the relatively slow time scale of the SQUID experiment. To account for the observed magnetic behavior in **4**−**6**, the lattice must be soft enough to allow for the coordination sphere expansion but possess some mechanism of stability. The limiting cases of soft and hard lattice packing are thus both expected to show no conversion in response to irradiation, consistent with the behavior observed for the complexes with the smallest substituents, **1** (H) and **3** (Me), and the larger substituent, **2** (OMe). For those substituents resulting in a moderate hardness of the lattice, there is enough intermolecular space to allow for the expansion accompanying the valence tautomeric conversion. There is also a close enough packing to provide a mechanism to lock the structure in the newly expanded confirmation through intermolecular close contacts. It appears that in this way the size of the substituents affords a remote control over the lattice packing, resulting in a "Goldilocks" substituent effect. Complexes **4**−**6** share similar effective van der Waals volumes (Table 3) and afford the right modulation of the lattice packing to allow metastability of the photogenerated form, where the necessary range of VdW volume is ca. 14−17 cm$^3\cdot$mol^{-1}.[49]

It is thus important now to account for the relevant intermolecular contacts responsible for the observed behaviors. In a previous report on the photoinduced valence tautomerism of **4**, we proposed a mechanism of stability primarily due to the presence of close intermolecular hydrogen bonding (C−H$\cdots$N$_{-CN}$ and C−H$\cdots$O$_{diox}$) in the lattice, supported by the anisotropic distortion of the unit cell parameters in the structures of the *ls*-Co^{III} and *hs*-Co^{II} forms.[11] The crystalline

(49) Bondi, A. *J. Phys. Chem.* **1964**, *68* (3), 441–451.

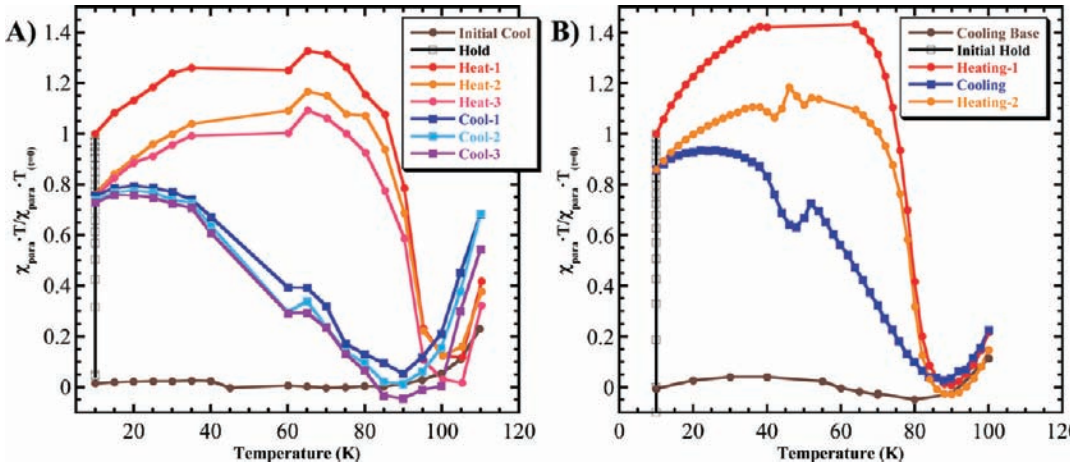

Figure 11. Normalized variable-temperature magnetic susceptibility cycles of **4**. (A) Constant irradiation from 10 to 110 K (2 K/min rate); first cooling curve shows baseline behavior with sample introduced at 150 K and no irradiation. (B) Constant irradiation from 10 to 100 K (0.1 K/min rate); first cooling curve shows baseline behavior with sample introduced at 150 K and no irradiation. The data from 45 to 55 K are obscured due to a phase transition in oxygen trapped in the sample cavity and have been omitted.[44–46]

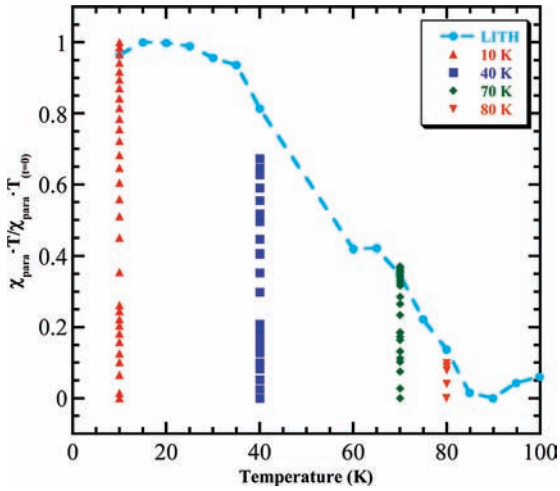

Figure 12. Normalized variable-temperature magnetic susceptibility of **4** under constant irradiation at 10, 40, 70, and 80 K demonstrating the maximum conversion ratio. A cooling LITH curve is included for reference. The data from 45 to 55 K are obscured due to a phase transition in oxygen trapped in the sample cavity and have been omitted.[44–46]

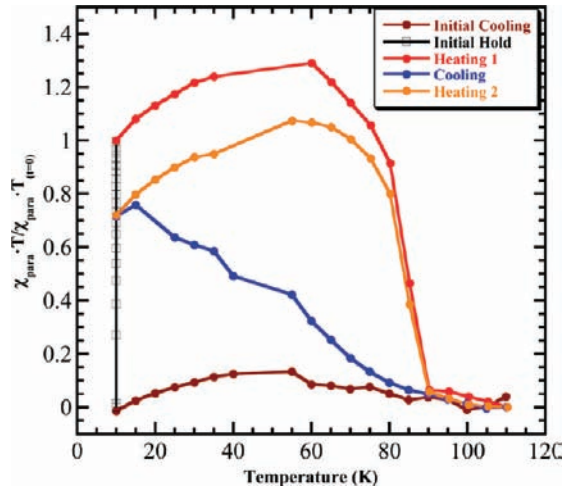

Figure 13. Normalized variable-temperature magnetic susceptibility cycles of **6**. Constant irradiation from 10 to 110 K (2 K/min rate); the first cooling curve shows baseline behavior with sample introduced at 150 K and no irradiation. The data from 45 to 55 K are obscured due to a phase transition in oxygen trapped in the sample cavity and have been omitted.[44–46]

distortion and similar hydrogen-bonding contact distances in the two tautomeric forms speak to the importance of this hydrogen-bonded lattice in stabilizing both forms. This hydrogen bonding can act to provide a mechanism to facilitate the *ls*-$Co^{III} \rightarrow$ *hs*-Co^{II} conversion, by lowering the activation barrier for Co−N and Co−O bond length elongation. The hydrogen-bonded lattice can similarly stabilize the expanded *hs*-Co^{II} tautomer. Inspection of the structures of **5** and **6** reveals very similar intermolecular bonding interactions (Figure 15).

Complex **6** shares the same space group as **4** ($P2_1/c$), and as such demonstrates similar molecular packing (Figure 15A/B). As expected, the C−H···O_{Nitro} and C−H···O_{diox} contacts are 2.41 and 2.39 Å, very similar to those in **4**.[11,50] However, the C−H···O_{diox} contact is ca. 0.09 Å longer, and the C−H···O_{Nitro} contact suffers from bond rotation about the C−N bond. Both of these effects can act to limit the effect of these hydrogen bonding interactions. Complex **5** possesses a different space group ($P\bar{1}$) and demonstrates slightly different packing than **4** and **6** (Figure 15C/D). Inspection of the intermolecular contacts reveals a C−H···O_{diox} contact of 2.36 Å, but there are no obvious C−H···Br contacts within the sum of VdW radii (3.05 Å).[50] Upon closer inspection, the −Br substituent directly faces two aromatic π-systems, potentially forming two weak Br−π interactions: (1) the dioxolene face along the Br−C bond axis and (2) the pyridine face parallel with the Br−C axis. The Br···π_{aryl} interaction is directly pointed to a carbon in the π-system, where the distance is 3.29 Å, well within the sum of VdW radii of 3.55 Å.[49–51] For the Br··· $\pi_{pyridyl}$, the −Br is nearly centered above the pyridyl ring, where the distance from the plane of the ring to the −Br is ca. 3.53 Å, an acceptable distance for this type of interaction.[50,51]

Examination of the structures of **1**−**3** did not demonstrate close molecular contacts similar to those found in **4**−**6**. Complex **2** shares the same space group as **4** and **6** ($P2_1/c$), yet the C−H···X contacts are different. The C−H···O_{diox} contact to

(50) Desiraju, G. R.; Steiner, T. *The Weak Hydrogen Bond in Structural Chemistry and Biology*; Oxford University Press: New York, 1999.

(51) Broder, C. K.; Howard, J. A. K.; Keen, D. A.; Wilson, C. C.; Allen, F. H.; Jetti, R. K. R.; Nangia, A.; Desiraju, G. R. *Acta Crystallogr.* **2000**, *B56* (6), 1080–1084.

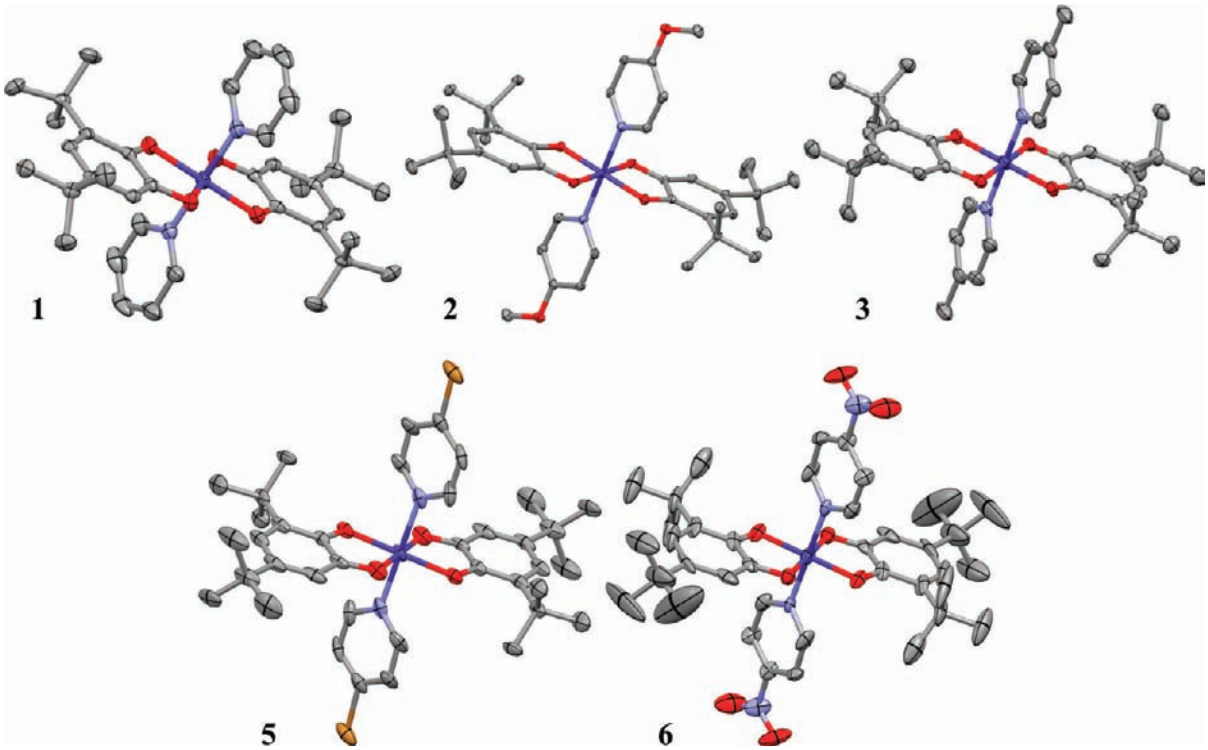

Figure 14. ORTEP structure of complexes **1**−**3**, **5**, and **6**; hydrogens and solvent molecules have been omitted for clarity.

Table 3. Effective van der Waals Volumes for the Substituents in **1**−**6**[a]

Substituent	Effective van der Waals Volume[49] (V_W, $cm^3 \cdot mol^{-1}$)
−H, **1**	*3.50*
−OMe, **2**	*18.21*
$-CH_3$, **3**	13.67
−CN, **4**	14.70
−Br, **5**	14.60
$-NO_2$, **6**	16.80

[a] Italicized values calculated from group contributions.

the pyridyl ring is ca. 2.43 Å, which, while within the sum of the VdW radii,[49] differs by ca. 0.13 Å from the distance in **4**. Also, the apparently more relevant substituent distance of C−H···O_{-OMe} is ca. 2.70, which is right at the limit of the VdW sum for O and H (2.72 Å)[49] and also subject to interruption by the methyl group from bond rotation. The structures of **1** and **3** share a different space group, $P2_1/n$, which affords a slightly different packing. A consequence of this packing is the loss of the C−H···O_{diox} contact found in **4**−**6** and longer distances to the pyridyl substituent. Also, the pyridyl substituents in **1** and **3** do not form good hydrogen bonds (−H and −Me), while there are some possible C−H···π_{aryl} interactions of ca. 3.0 Å which seem to be of little consequence to the metastability.

Given the differences in intermolecular interactions in these systems, it seems reasonable to reevaluate the differences in the thermal valence tautomeric conversion behavior for **4**−**6**. Complex **4** presents the shortest C−H···X contacts (C−H···N_{-CN} = 2.45 Å and C−H···O_{diox} = 2.30 Å, Co^{III} form) and is least subject to distortion (due to the linearity of CN), which should be manifest in the strongest facilitation of *ls*-Co^{III} → *hs*-Co^{II} conversion (T_{onset} = ca. 100 K).[11] Complex **6** is the most similar to **4** in the C−H···X contact distance, as they share a space group; however the dioxolene contact is slightly longer (Δ = 0.09 Å), and the $-NO_2$ contact is subject to bond rotation which can limit its influence (T_{onset} = ca. 130 K). Finally, complex **5** possesses only one C−H···O contact with the dioxolene, again longer than that in **4** (Δ = 0.06 Å), but lacks good C−H···Br interaction and possesses two nominally weaker Br··· π_{face} interactions (T_{onset} = ca. 150 K). This trend suggests that the presence and strength of these intermolecular interactions play a very large role in the stabilization of *hs*-Co^{II} and facilitation of the thermal *ls*-Co^{III} → *hs*-Co^{II} conversion. This also speaks to the importance of the hydrogen bonding to the pyridyl substituent in the facilitation of the *ls*-Co^{III} → *hs*-Co^{II} conversion, where the onset temperatures for conversion follow the trend **4** < **6** < **5**, in line with the observed hydrogen bonding interactions to the pyridyl substituent.

Some of the crystal structures were found to contain solvents of crystallization (toluene) trapped in the lattice, the incorporation of which could affect the photoinduced and thermal activity. To verify the behavior in both the pure molecular crystals (**4a**) and toluene-solvate crystals (**4b**), the data sets were compared on both for the 4-cyanopyridine system. X-ray structures and unit cells were used to check different crystal growths to identify batches of **4a** and **b**, which were then immediately subjected to photoirradiation and thermal cycling to avoid any potential atmospheric solvent loss. Both samples were excited to the *hs*-Co^{II} form and trapped, demonstrating similar stabilities and conversion maxima. The impact on the thermal conversion was also of interest, as the presence of toluene appeared to diminish the cooperativity in the transition ($T_{1/2}$ = ca. 160 K vs 110 K), yet had little effect on the onset temperature (T_{onset}). Figure 16 is a comparison of the heating and cooling cycles of two samples of **4**, one with toluene in the lattice and one without. The inclusion of toluene serves to "soften" the lattice and allows for a less cooperative transition, where, in the pure molecular lattice, a single *hs*-Co^{II} → *ls*-Co^{III} conversion event demonstrates

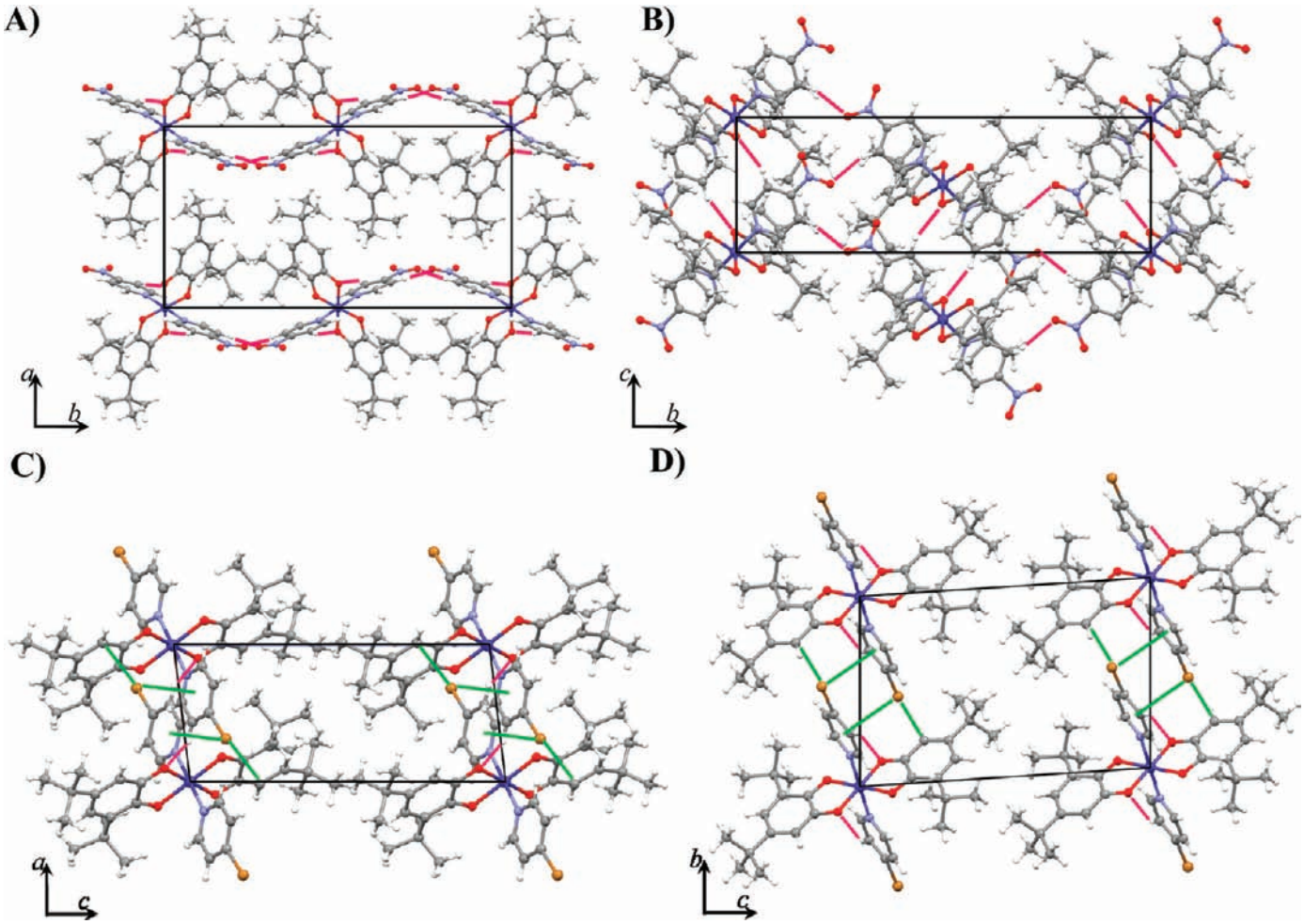

Figure 15. Crystal packing diagrams of **5** (bottom) and **6** (top). Views (A) and (B) for **6** are shown down the *c*-axis and *a*-axis, respectively, where views (C) and (D) for **5** are shown down the *b*-axis and *a*-axis, respectively. Relevant H-bonding interactions are represented as purple contacts, and π-face interactions as green contacts.

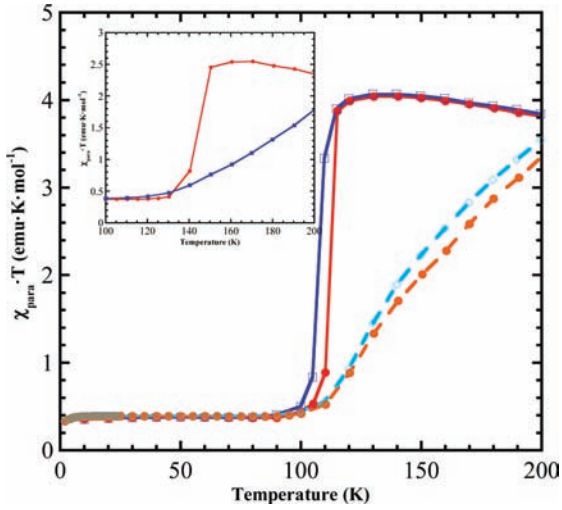

Figure 16. Variable-temperature magnetic susceptibility plotted as $\chi_{para} \cdot T$ vs T for samples of **4a** (red ●/dark blue □) and **4b** (orange ●/light blue □). Inset: Comparison of solvated (●) and nonsolvated (■) samples of **6**.

strong cooperativity and cascades rapidly through the lattice, affording the precipitous drop in $\chi_{para} \cdot T$.[23] This toluene−solvate behavior observed in **4b** is also very similar, in the gradual increase in $\chi_{para} \cdot T$, to that observed initially for **6**. The inset to Figure 16 shows subsequent data collected on a sample of **6** devoid of solvent, again demonstrating a much more cooperative transition and little effect on T_{onset}.

Inspection of the crystalline packing in these lattices reveals that the toluene molecules insert between the molecular layers, very closely resembling the solvent-free packing (Figure 17). The space group is $P2_1/c$ in both systems (**4a** and **b**), and they differ primarily in the *a*-axis length (ca. 7 Å vs ca. 15 Å) and the cell volume (ca. 1900 Å^3 vs ca. 2480 Å^3).

The inclusion of the toluene solvent into the lattice provides a layer, separating the crystal into sheets, where only the *para*-*tert*-butyl interlayer interactions may be weakened. Both of the relevant hydrogen bonding interactions are maintained within the molecular layers, where the C−H···N and C−H···O contacts are 2.74 Å and 2.29 Å in **4b** (compared to 2.48 Å and 2.30 Å in **4a**), still within the sums of the VdW radii. The increase in the C−H···N distance could easily account for the more gradual thermal conversion observed in **4b** by weakening the cooperativity within the lattice. This gradual conversion may also be due to the separation of the molecular layers, allowing the layers to flex within the crystal, which would in turn weaken the intermolecular interactions. Inclusion of more toluene layers into the lattice should act to continue to raise the $T_{1/2}$ of valence tautomeric conversion, allowing the molecular layers freedom to shift within the *b*−*c* plane, imparting a shear force to the hydrogen bonds responsible for the novel behavior. It is this *b*−*c* plane that contains the primary interactions responsible for

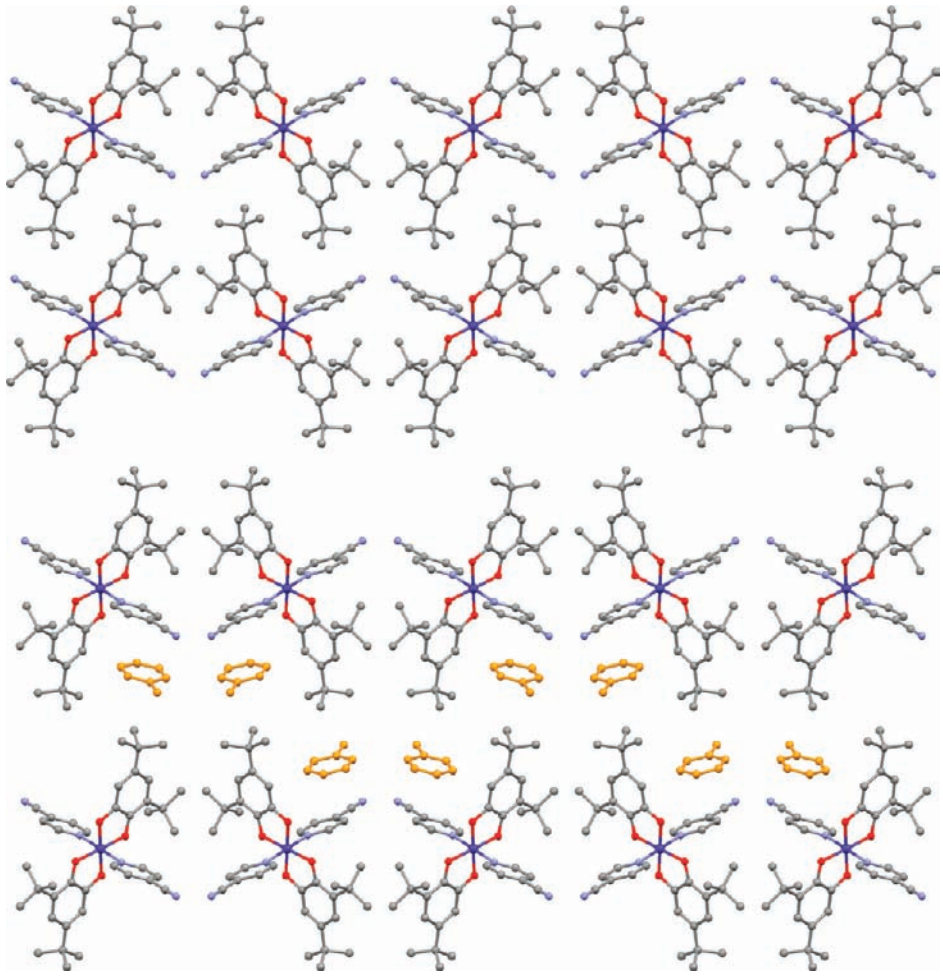

Figure 17. Crystalline packing for **4a** (top) and **4b** (bottom) highlighting inclusion of toluene (orange) into lattice.

the anisotropic cell distortion in the conversion of *ls*-Co^{III} → *hs*-Co^{II}.[11] Ultimately, a limit of solvation may be reached, where enough toluene is intercalated into the lattice to isolate the molecular layers and now allow them to fragment along the hydrogen bonding interactions into isolated (solvated) molecules. It is in this limit that the behavior should now be dominated by the molecular properties, as the solid-state facilitation effects have been removed, and the observed thermal behavior for **4**−**6** should resemble that of **1**−**3** (Figure 1A).

The observation of photoinduced valence tautomerism and metastability in both solvated and nonsolvated forms of **4** suggests strongly that it is the intermolecular interactions within this molecular layer that are responsible for the observed behavior and the interlayer (*para*-*tert*-butyl) interaction only acts to magnify the behavior and harden the lattice, resulting in a more cooperative thermal transition. The inclusion of toluene in the lattice does have an effect on the thermal behavior, by acting to soften the lattice to allow for a more gradual, less cooperative conversion.

Conclusions

Valence tautomers of this structural type represent a new archetype in photoinduced valence tautomerism, demonstrating a highly stable photogenerated Co^{II} form, accessible also through rapid thermal quenching. The thermal valence tautomerism for **4**−**6** is accompanied by hysteresis and is very sensitive to the hardness of the lattice. The thermal stability of the photogenerated forms of **4**−**6** represent the highest T_{decay} reported to date for photoinduced cobalt valence tautomerism, and the kinetic stability and decay mechanism support a self-accelerated decay process. The presence of new light-induced thermal hysteresis is also observed, the first such example in a cobalt valence tautomeric complex. The highly cooperative nature of these behaviors is reliant primarily on the intermolecular hydrogen-bonding network within the pure moleculer lattice. Disruption of this lattice effect in **4**−**6**, through lattice softening via solvent intercalation or solvation, results in relaxation or elimination of both the thermal and photoinduced behavior reverting to the expected behavior observed for **1**−**3** and other structurally similar complexes.

Acknowledgment. D.A.S. thanks the National Science Foundation (CHE-0345263/0910585) for financial support. The authors wish to acknowledge Dr. Jeff W. Kampf of the University of Michigan for X-ray crystallographic data collection and refinement, Prof. Thomas Meyer and Dr. Kyle Brennaman for use of their Shimadzu UV-3600 spectrometer, and Prof. Andreas Hauser for valuable discussions.

Supporting Information Available: Crystallographic details (CIF), saturation magnetization, electronic absorption spectra. This material is available free of charge via the Internet at http://pubs.acs.org.

JA101957C